A multifunctional hydrogel fabricated via ultra-fast polymerization by graphene oxide-adsorbed liquid metal nanodroplets

A multifunctional hydrogel fabricated via ultra-fast polymerization by graphene oxide-adsorbed liquid metal nanodroplets

Yaotian Su[a], Jiawei Zhao[b], Wenwei Zhan[a], Haocheng Yuan[a], Lingyun Wu[a], Gang Sui[a], Hongtao Zhang[c]

[a]State Key Laboratory of Organic-Inorganic Composites, College of Materials Science and Engineering, Beijing University of Chemical Technology, Beijing 100029, China

[b]SINOPEC Beijing Research Institute of Chemical Industry, China

[c]Department of Materials, Loughborough University, Leicestershire, UK

Abstract

Graphene structures have never been found to play a role in accelerating fabrication of functional hydrogels. In this work, it is initially discovered that multifunctional hydrogels are fabricated via ultra-fast polymerization (~minutes) by graphene oxide-adsorbed liquid metal nanodroplets (LMNPs@GO) vs. by conventional approaches (~hours/days). LMNPs@GO are used to rapidly initiate and further cross-link polyacrylic acid (PAA) chains into a three-dimensional (3D) network without any extra molecular initiators, cross-linkers, heat source, and/or protective gas. The polymerization process with LMNPs@GO is extremely faster than that without GO involved (20 s vs. 4 h of prepolymer formation, and then 10 min vs. 3 days of crosslinking) for free radical polymerization of PAA hydrogels. The resulting hydrogel with 2 wt% reduced graphene oxide (rGO) exhibits 600% increase in tensile strength and 950% enhancement in conductivity, as well as excellent self-healing capabilities, in comparison with that of the pure PAA. The sensitivity studies show its great potential for the application of flexible sensors. Furthermore, the hydrogel possesses good dissolving properties, which is greatly beneficial for recyclability of the LM. This creative study not only broadens a novel application of graphene for making advanced multifunctional polymer materials, but also provides a brand-new route to realization of ultra-fast manufacturing technology that is significantly promising for industrial production in wearable devices.

1. Introduction

With the advancement of artificial intelligence, flexible strain sensors are receiving tremendous attention for their substantial applications in electronic skins, personalized healthcare monitoring, and human–machine interaction field [1], [2], [3], [4], [5]. Recently, various functional soft materials have been widely investigated for the fabrication of flexible wearable strain sensors due to their excellent electronic properties, tunable mechanical properties, and remarkable biological characteristics [6], [7], [8], [9], [10]. Polymer hydrogels, consisting of a large amount of water and three-dimensional (3D) polymer networks, not only possess good flexibility similar to bio-tissues, but also exhibit excellent stretchability, self-healing ability, and conductivity over conventional "hard" polymeric materials, making them ideal candidates for soft matrices of wearable devices [11], [12], [13], [14], [15], [16]. Traditional strategies for preparation of hydrogels are based on free radical polymerizations, in which heat source and protective gas (nitrogen or argon) are necessary conditions to ensure the occurrence of the polymerizations [17], [18], [19], [20]. However, these strategies are usually energy-and time-consuming and demand for complicated operations, which are hardly suitable for industrial production, because typical free radical polymerization reactions are generally completed in a time scale of hours at least. Besides, if nanofillers as ingredients to be incorporated in the polymerization systems for improving the performance of hydrogels, the reaction efficiency may further decrease due to the trapping or quenching effect of nanofillers on free radicals [21]. Hence, it is highly desirable to develop a fast polymerization method to prepare multifunctional hydrogels with excellent mechanical, self-healable and conductive properties.

Eutectic gallium indium (EGaIn), a nontoxic liquid metal (LM) alloy at room temperature, can be incorporated into elastomers or hydrogel to fabricate highly stretchable, mechanically robust, soft multifunctional composites with high thermal and electrical conductivity. These characteristics make it suitable for applications in soft robotics and self-healing electronics [22], [23], [24], [25], [26]. A recent study reported that EGaIn liquid metal nanoparticles (LMNPs) could initiate the polymerization of vinyl-based monomers such as acrylamide under sonication in an aqueous solution without the need for conventional molecular initiators [27]. This phenomenon was attributed to the odd electron species of atomic configuration of Gallium ([Ar] $3d^{10}4s^24p^1$) for providing a source of unpaired electrons that can potentially act as radical initiators for polymerization. Unfortunately, due to the intrinsic high density of LM, the LMNPs cannot be well dispersed in hydrogels and unavoidably precipitate with the prolonged reaction time. In addition, the gelation process of the LMNPs-initiated reaction was very slow (>7 days), which severely impeded the industrial application requiring short production cycles. An improved strategy by adding EGaIn LMNPs to catalyze persulfate radical initiators for the acrylic acid (AA) fast polymerization was reported [28]. Although the polymerization efficiency was tremendously enhanced, the addition of molecular initiators inevitably introduced impurities in the hydrogel system, which was not beneficial for the application in biological field.

Graphene oxide (GO) is a two-dimensional derivative of exfoliated graphite under strong oxidizing conditions. It has prominent characteristics such as sp2 planar structure, several nanometer thickness, a highly hydrophilic nature, and a high number of oxygen-containing functional groups such as hydroxy, carboxyl and epoxy, which have been envisioned to greatly benefit a wide range of promising applications [29]. Previous studies reported that by loading platinum (Pt) nanoparticles catalyst on the surface of GO, the catalytic efficiency was significantly enhanced because the large specific surface area of the GO nanosheets improved the dispersity of the Pt nanoparticles, guaranteeing its catalytic activity [30], [31]. Furthermore, commercially produced GO exhibits disrupted planar π-network structure, exhibiting phenol hydroxy and epoxide groups at the basal plane and carboxylic groups at the lateral edge, which renders its ability to capture the free radicals in the surroundings [32]. Therefore, it is reasonable to infer that the attendance of GO can have a positive effect on free radical polymerization.

Herein, for the first time, we discover that GO tremendously accelerates the polymerization process initiated by LMNPs. A very fast polymerization reaction of AA prepolymer formation occurs within 20 s, and then an ultra-robust polyacrylic acid (PAA) hydrogel is obtained within 10 min. In contrast, for the processes without GO involved, the time durations are 4 h for the formation of the AA prepolymer and then 3 days for obtaining the cross-linked hydrogels. The resulting hydrogel with 2 wt% reduced graphene oxide (rGO) exhibits 600% increase in tensile strength and 950% enhancement in conductivity, as well as excellent self-healing capabilities, in comparison with that of the pure PAA. Furthermore, the studies on dissolving property and sensitivity indicate that some of the LM can be recycled, and the hydrogel is well applicable for strain sensors. The mechanism behind the fast polymerization phenomenon is systematically investigated via combination of experiment and density function theory (DFT) simulation. This novel strategy can be extended to almost all types of LM-radical polymerized hydrogels, which holds great potentials for the industrial production of wearable sensor devices.

2. Experimental

2.1. Materials

Graphene oxide (GO, average sheet size is > 2 μm) was provided by Xianfeng Nanomaterials Tech. Co., China. Eutectic gallium indium (EGaIn, mass ratio Ga:In = 75/25) liquid metal was obtained from Changsha Santech Materials Co., China. Luminol (>99%), acrylic acid (AA, >98%), potassium iodide (KI, >99.9%), soluble starch (>99%), ammonium persulfate (APS, >99.9%), sodium thiosulfate (Na_2S_2O3, >99.9%) were all purchased from Aladdin Co., USA.

2.2. Preparation of LMNPs@rGO/PAA hydrogel

LMNPs@GO hybrid nanosheets were firstly fabricated in this procedure. 150 mg EGaIn was dissolved in 20 ml deionized water and ultrasonicated for 3 min. A certain amount of GO was then added in the above dispersion and ultrasonicated for another 2 min to form LMNPs@GO hybrid nanosheets. After the solution cooled down to the room temperature, AA monomers was introduced to the mixture. The weight percentage between GO and AA was 0.0 wt%, 0.5 wt%, 1.0 wt%, 1.5 wt% and 2.0 wt%, respectively. The mixture was stirred for 1 min and then fast transferred to the Teflon mold. The robust LMNPs@rGO/PAA hydrogel can be obtained within 10 min and coded as 0.0 wt% LMNPs@rGO/PAA, 0.5 wt% LMNPs@rGO/PAA, 1.0 wt% LMNPs@rGO/PAA, 1.5 wt% LMNPs@rGO/PAA, 2.0 wt% LMNPs@rGO/PAA.

2.3. Characterizations

The type of charge on the graphene oxide (GO) and liquid metal nanoparticles (LMNPs) were distinguished by Zeta potential system (Zetasizer 3000, Malvern Instruments, Britain). The morphologies of GO adsorbed LMNPs hybrid (LMNPs@GO) nanosheets, dried LMNPs@rGO hydrogel and rGO nanosheets dissolved from LMNPs@rGO/PAA hydrogel were examined by transmission electron microscopy (TEM, Tecnai, model G220, USA) and scanning electron microscope (SEM, JSM-7401F, JEOL, Japan) equipped with energy dispersive X-ray spectroscopy (EDS). The fast polymerization process was monitored by torque rheometer (DHR3, TA, USA) and infrared thermal imager (DS-2TPH13-3VAF, HIKVISION, China). The free radicals generated in the polymerization process were characterized by electron paramagnetic resonance instrument (Bruker EMXplus X-band EPR, Bruker, Germany) combining with iodometric titration and luminol detection method. The molecular weight of the hydrogel was measured using gel permeation chromatography (GPC, Agilent PL-GPC220, USA). The reduction of GO was characterized by the X-ray photoelectron spectroscopy (XPS, Thermo ESCALAB 250, Thermo Fisher Scientific, USA), Raman spectra (DXR3, Thermo Scientific DXR2, USA) and X-ray diffraction (XRD, XRD-7000, Shimadzu, Japan). The mechanical properties of the hydrogel were tested by universal testing machine (Instron-1121, UK). The samples were molded into cylinder shape 5 mm (diameter) × 30 mm (length) with a loading rate of 50 mm/min. The gauge length between the clamps was 10 mm. The conductivity of hydrogels was measured by alternating current impedance spectroscopy (ESI) and AVO meter. The real-time electrical signals of the strain sensors were recorded by the electrometer (Keithley 6514, USA) under resistance-mode.

3. Results and discussion

3.1. Preparation of LMNPs@GO hybrid initiators

An electrostatic self-assembly method is operated to synthesize the LMNPs@GO nanosheets and the mechanism is shown in Fig. 1 a. EGaIn is firstly sonicated into LMNPs in the deionized water. GO aqueous suspension is then slowly added to the LMNPs mixture under stirring. Due to the distinction of Zeta potential for LMNPs and GO nanosheets (Fig. 1 b), the LMNPs with positive charge are easily adsorbed on the surface of the negatively charged GO nanosheets.

The negative charge of GO is attributed to the oxygen-containing functional groups on the surface of the nanosheets, while the positive charge on the LMNPs come from the gallium oxide hydrate which can capture the hydrogen proton in the water solution [33]. The weight ratio between LMNPs and GO dominates the polymerization in this reaction system as it influences the dispersion stability of LMNPs@GO hybrid nanosheets in water, which determines the occurrence of fast polymerization and the final properties of the hydrogel product. Fig. 1 c shows the dispersion state of LMNPs@GO with different weight ratio of LMNPs and GO. For pure LMNPs solution without adding GO. The dispersion of LMNPs is not stable and after 48 h nearly all LMNPs are sedimented at the bottom of the vial. With the increment of GO (LMNPs/GO = 150/40 and 150/45), the LMNPs@GO gradually appears dispersion stability within short period of time (24 h), however the phase separation still occurs (48 h) due to the saturated adsorbing ability of GO. Further increasing the concentration of GO will improve the dispersion of LMNPs@GO, which is beneficial for the initiation of the polymerization. It should be noted that the content of GO cannot exceed 200 mg (13 mg/ml), because too much GO will cause the gelation phenomenon as shown in Fig S1. Consequently, the concentration of GO is optimized from 50 mg (3.3 mg/ml) to 200 mg (13.3 mg/ml), which guarantees the fast polymerization and excellent dispersion stability of LMNPs@GO in the hydrogel matrix. The self-assembled LMNPs@GO exhibits good integrity, and all LMNPs are perfectly adsorbed on GO sheets as shown in Fig. 1 d. The LMNPs adsorbed on the surface of GO all show perfect spherical shape compared with those ultrasonicated in water without GO nanosheets which exhibit short rod-like and other irregular shape (see Fig S2). It has been reported by previous research that Gallium-based LMs were prone to being oxidized under the low oxygen partial pressure, and they can also be easily completely oxidized into GaOOH [34]. However, after adsorption on the surface of GO, the LMNPs can be protected by the intact GO shell which prohibits the oxidation of LMNPs [35]. The magnified TEM images (Fig. 1 e) also elucidates that some of the LMNPs are well encapsulated by the GO nanosheets which is more effective to restrain the further oxidation of LMNPs core. The protective effect of GO shell is largely attributed to its low oxygen permeability and hydrophobicity [35]. Besides, the metal ions can penetrate between the layers of graphene for mass transfer, owing to that the ionic radius of metal elements is typically smaller than the interlayer spacing of GO. Therefore, LMNPs@GO can be a desired platform for the galvanic replacement reaction [36]. The microstructure of filtrated dried LMNPs@GO is characterized as shown in Fig S3. The high-resolution SEM image (Fig S3 b) indicates that the LMNPs are uniformly inserted into the interlayer of GO. This uniformity is further demonstrated by the EDS mapping of element gallium and indium as shown in Fig S3 c and d. The uniform distribution of LMNPs increases the active sites for free radical reactions which is beneficial for the fast polymerization of PAA hydrogel.
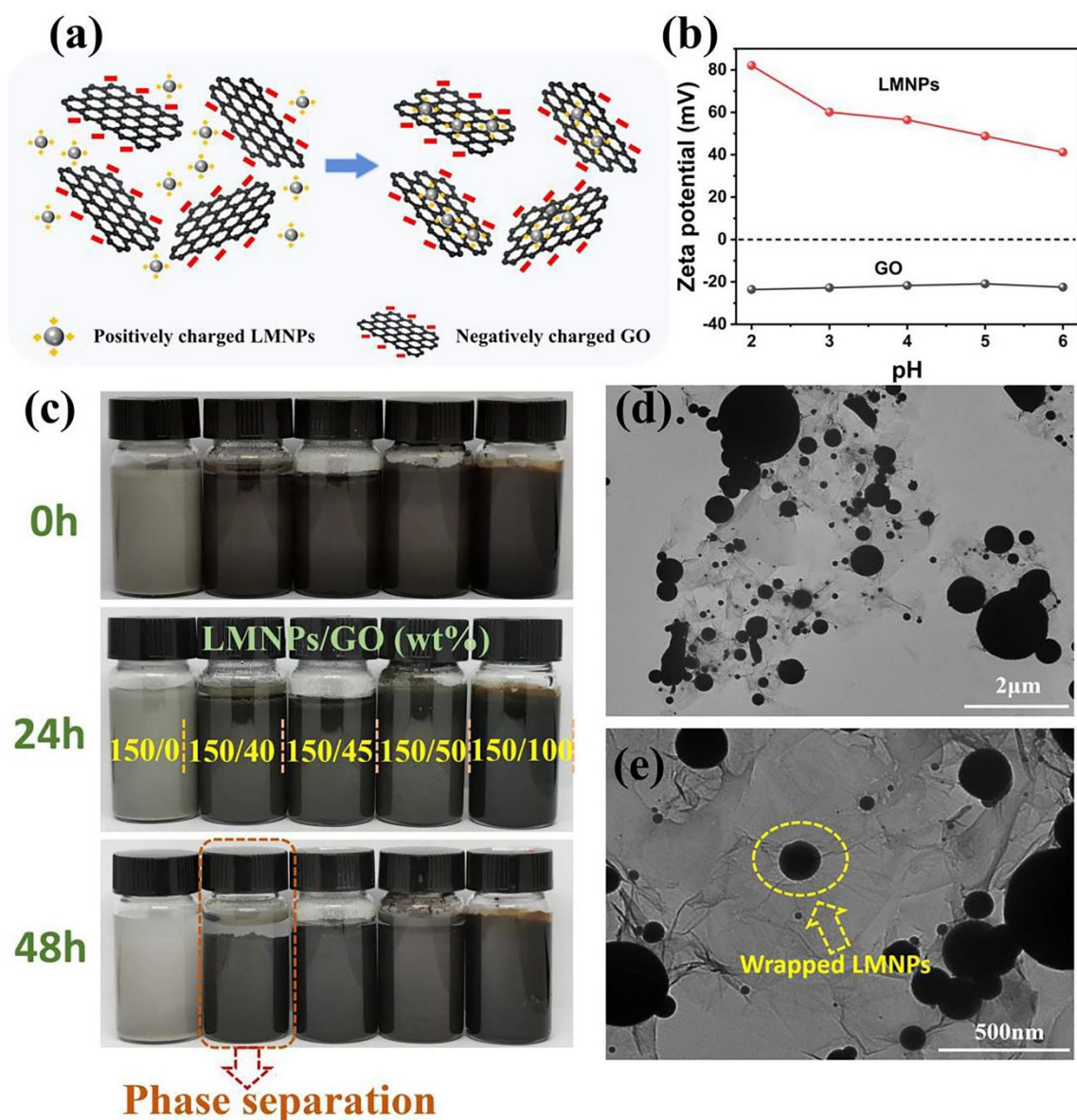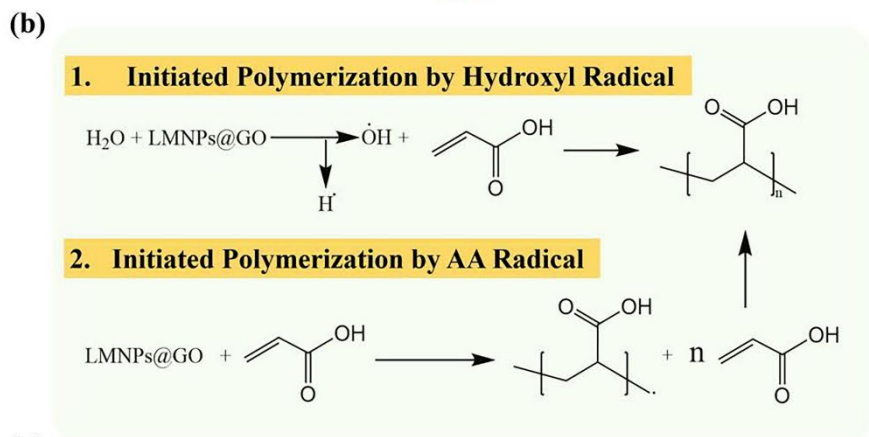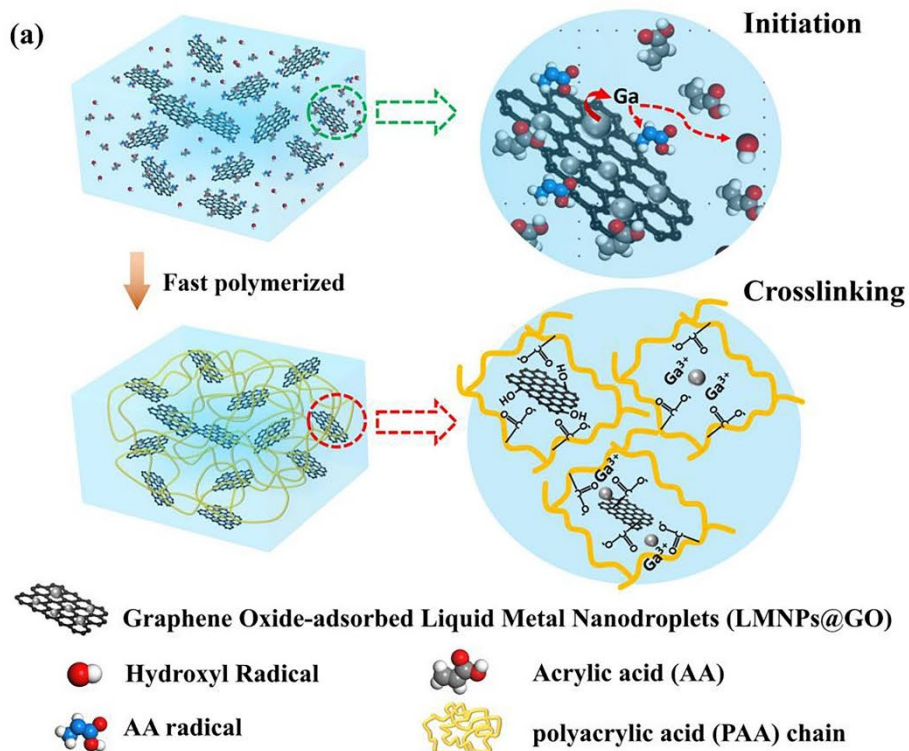
Fig. 1. Fabrication and characterization of LMNPs@GO nanosheets. (a) Mechanism diagram. (b) Zeta potential of GO and LMNPs in the water. (c) Dispersion state of LMNPs@GO nanosheets with different LMNPs/GO weight ratio at various time intervals. (d) and (e) TEM images of LMNPs@GO nanosheets.

3.2. Rapid preparation of LMNPs@rGO/PAA hydrogel

The graphene oxide-adsorbed liquid metal nanodroplets initiated polyacrylic acid (LMNPs@rGO/PAA) hydrogel is prepared by a rapid radical polymerization of AA monomers with the existence of LMNPs@GO nanosheets. The scheme for the rapid preparation of LMNPs@rGO/PAA hydrogels is shown in Fig. 2. The initiation reaction is induced by the free radicals generated by the LMNPs due to the odd electron species of atomic configuration of Gallium ([Ar] 3d104s24p1). The free radicals can be divided into two categories as shown in Fig. 2 a and b. The first species are hydroxyl free radicals which exist in the water, which can directly initiate the polymerization of AA monomers; the second species are AA radicals which are directly initiated by LMNPs. Because most of the LMNPs are adsorbed on the surface of

GO, the initiation reaction will be induced around GO and the resultant hydrogel is well crosslinked by GO. For a hydrogel system containing GO and Ga3+, the 3-dimensional network structure is constructed through three sorts of crosslinking points as shown in Fig. 2 a: (i) the first cross-linking points are Ga3+ creating ionic cross-linking among PAA chains; (ii) the second cross-linking points are GO nanosheets linking PAA chains through metal coordination. (iii) the third cross-linking points are the hydrogen-bond interaction between the oxygen-containing functional group on the surface of GO and the carboxyl groups on the PAA chains. The non-covalent crosslinking points endow the hydrogel with excellent mechanical, self-healing and dissolvable properties which guarantees its further application. The proportion of LM is based on if the initiation reaction can be induced and the dispersion state of LMNPs or LMNPs@GO in the reaction system. For pure LMNPs initiated PAA hydrogel (LMNPs/PAA), the content of LM exceeding 1.5 wt% (LMNPs/AA) will cause the aggregation and sedimentation of LMNPs (Fig S4 a), which is detrimental to the initiation of the polymerization so that the mechanical properties are deteriorated (Fig S4 b). While the content of LMNPs is less than 1.5 wt%, the gelation process will not happen, or the gelation time is too long (>14 days), which is not helpful to our study. The optimized concentration of AA monomers has been systematically investigated by Ma et al. [27]. Consequently, the specific proportion of the ingredient of the synthetic hydrogel is listed in Table S1. Although the LMNPs@GO nanosheets maintain well dispersibility, an intense stirring environment is badly needed to ensure their dispersion and excite full contact with AA monomers. The prepolymer of the hydrogel containing LMNPs@GO can be formed within 20 s, and in this process the solution becomes sticky as shown in Fig. 2 c (II). Approximately 4 min later, the system starts releasing a lot of heat, which indicates the automatic acceleration phenomenon and crosslinking during the reaction process. The system returning to room temperature represents the termination of the reaction. Subsequently, a LMNPs@rGO/PAA hydrogel with desirable mechanical properties is successfully prepared and a 2 kg load is easily lifted by the cylinder (Φ5 mm × 30 mm) hydrogel sample (Fig. 2 c (II)).

(a)

Initiation

Crosslinking

Graphene Oxide-adsorbed Liquid Metal Nanodroplets (LMNPs@GO)

Hydroxyl Radical

Acrylic acid (AA)

AA radical

polyacrylic acid (PAA) chain

(b)

1. **Initiated Polymerization by Hydroxyl Radical**

H_2O + LMNPs@GO $\longrightarrow$ $\dot{O}H$ + ... $\longrightarrow$ ...

$\dot{H}$

2. **Initiated Polymerization by AA Radical**

LMNPs@GO + ... $\longrightarrow$ ... + n ...

(c)

I. Polymerization with LMNPs:

Without GO

LMNPs+AA solution

4hrs initiated

prepolymer

3 days crosslinked

Hydrogel

LM aggregation

II. Polymerization with LMNPs@GO:

With GO

LMNPs@GO+AA solution

20 sec initiated

prepolymer

10 min crosslinked

Hydrogel

No LM aggregation

2kg

Good mech property

Fig. 2. Preparation of LMNPs@rGO/PAA hydrogel. (a) Scheme for the rapid preparation of LMNPs@rGO/PAA hydrogels. (b) Reaction mechanism for the polymerization of AA monomers. (c) Comparison of gelation process between LMNPs/PAA (I) and LMNPs@rGO/PAA (II) hydrogel.

During the gelation process, ionically conductive supramolecular PAA-hydrogel networks and electronically conductive LMNPs/rGO hybrid networks are formed simultaneously in short period times (10 min), which guarantees the better dispersion of nanofillers. As shown in Fig S5, the LMNPs aggregations and fragment are dictated by yellow arrows from Fig S5 d and e. In comparison, for LMNPs@rGO/PAA hydrogel containing 2 wt% rGO, LMNPs with smaller size and better distribution can be observed which demonstrates the LMNPs in LMNPs@rGO/PAA hydrogel have better dispersity. The better dispersion of LMNPs can also be reflected by the morphology of LMNPs@rGO/PAA hydrogel dried under vacuum freeze dehydration. The aggregation of LMNPs can be observed from the morphology of PAA without adding GO (Fig S6 a), while for LMNPs@rGO/PAA hydrogels the LMNPs are invisible which implies the LMNPs have been well-dispersed in the PAA matrix. The poor dispersion state of LMNPs in the hydrogel without adding GO can be seen by the digital photos as shown in Fig. 2 c. It can be observed from Fig. 2 c (I) that the as prepared LMNPs/PAA hydrogel molded into "number" shape displays metal luster on the surface, which suggests the LMNPs have precipitated to the bottom of the mold in the gelation process due to the slow change of viscosity during the experimental process. As an active metal, it has been reported that EGaIn can behave as a reactive filler to initiate the polymerization of AA monomers without adding molecular initiators, heat source and protective gas. However, the reaction time is too long and commonly 3 days or more are spent to obtain a hydrogel with available mechanical properties. This gelation process was firstly discovered by Ma et al. [27] and systematically investigated by Xu et al. [37]. In our experiment, we surprisingly discovered that with the addition of GO, the polymerization process can be tremendously accelerated and a robust LMNPs@rGO/PAA hydrogel can be well prepared within 10 min as shown in Fig. 1 c (II). The fast polymerization rate with those of other state-of-art hydrogels are compared in Table S4.

3.3. Gelation process and fast polymerization mechanism

To systematically investigate this fast gelation process, the rheology characterization is conducted to monitor the gelation time of the PAA hydrogel with different GO contents. Considering the gelation time of pure PAA incorporated with LMNPs without adding GO is too long, ammonium persulfate (APS) molecular initiator is employed to accelerate the polymerization process which has been reported in previous research [38]. The storage (G') and loss modulus (G'') versus oscillatory time sweep is shown in Fig. 3 a and b, respectively. The intersection of the curve with the x-axis represents the time of the fastest gelation moment. As is displayed, the hydrogel system containing LMNPs and APS has the longest gelation time of appropriately 550 s. For the system only containing LMNPs@GO, with the GO content increasing to 1.5 wt%, the gelation time declines to 44 s, which suggests the GO accelerates polymerization process and the formation of 3D gel network. By comparing this strategy with traditional method without GO (Fig. 3 c), the preparation efficiency is increased by 900%,

which is beneficial for the industrial production. It should be noted that when the GO content reaches 2 wt%, the gelation process is too fast to be determined so that the stable G' and G'' values are already found from the start of the measurement and remain constant in the range of time sweep study, showing that the gels very quickly obtain their final strength. During the gelation process, the system releases a lot of heat, which is reflected by infrared thermal imaging. Fig. 3 d displays the change of temperature in the gelation process. By recording the typical value, it is shown in Fig. 3 d that the temperature of the gelation system can reach a high value of 52°C within 500 s. After natural cooling, the robust hydrogel is obtained with excellent mechanical properties. The weight-average molecular weight (Mw) of the PAA hydrogel added with 2 wt% GO is 68,200 (Table S2 a), which is even higher than that initiated by APS + LMNPs (Mw = 47400, Table S2 b). Xu et al. [37] has systematically studied the gelation process of PAA hydrogel with the addition of LMNPs without using molecular initiators recently. The results indicated that the entire gelling process can be divided into four stages and the final gel with desirable mechanical properties should undergo 7 days which was much longer than the time consumed in our experiment. Because of lacking any other initiator in the gelling system of AA and LMNPs, it is believed that EGaIn in combination with sonication might produce free radicals and initiate AA polymerization, which was lately verified by Li et al. [39].
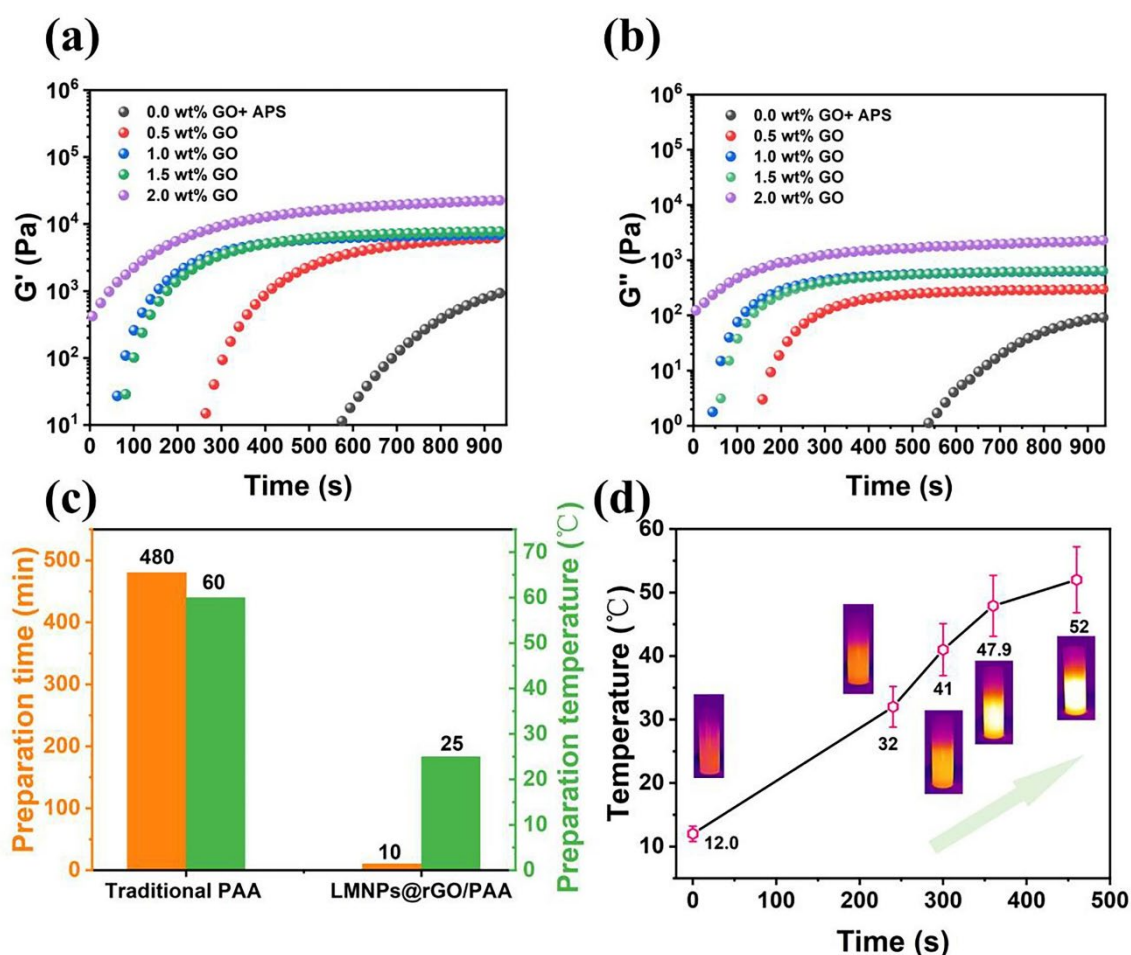

Fig. 3. Characterization of fast polymerization. (a) Storage (G') and (b) loss modulus (G'') variation versus oscillatory time sweep for the curing polyacrylic acid (PAA) hydrogel with different GO contents. (c) Comparisons of preparation time and temperature between traditional method and our method applied in this

experiment. (d) Variation of temperature in the polymerization process monitored by Infrared thermal imaging. The inset is the digital photos of Infrared thermal imaging at different time.

We speculates that the fast polymerization and gelation phenomenon in our research come from two possible reasons as follows: (i) the free radicals originated by LMNPs are captured by the GO nanosheets, which largely improves the specific area of the active site and lifespan of active species. (ii) the AA monomers are also adsorbed by the GO because of the oxygen-containing functional groups on the large sheets, thus significantly increases the contact probability between monomers and free radicals, facilitating the occurrence of initiation reaction. To prove the above hypothesis, the electron paramagnetic resonance (EPR) technique is employed to study the radicals formed in the polymerization process. A water-soluble diamagnetic spin trap 5,5-dimethyl-1-pyrroline-N-oxide (DMPO) is added to the mixture with different ingredients. For the mixture only containing LMNPs, a four-line spectrum (Fig. 4 c, spectral lines are marked with asterisks), shows 1:2:2:1 peak-to-peak intensity pattern with approximately equal interline splitting of 14.9 G. This is typical for the isotropic hyperfine couplings reported for $DMPO-OH\bullet$ spin adduct, implying that the addition of LMNPs can generate $\bullet OH$ free radicals. In comparison, for the water solution only added with GO, the spectrum displays only one resonance peak with g = 2.003, which is a typical peak of GO as reported in previous literature [40].By mixing LMNPs with different concentration of GO solution (labeled as LMNPs + GO-1 and LMNPs + GO-2, see Table S3.), the resonance peak of DMPO-OH• spin adduct cannot be observed and the characteristic peak is the same as GO spectrum. After adding AA monomers in the LMNPs + GO solution (labeled as LMNPs + GO + AA-1 and LMNPs + GO + AA-2, see Table S3.), the intensity of the characteristic peak is strengthened and still no other peaks can be observed. In general, the number of EPR lines (peaks) for a radical can be described by n = (2MI + 1), where M and I are the numbers of nucleus and spin equivalents, respectively [41]. The single EPR line for GO suggests that there is no equivalent nucleus directly bonded to the radicals. Therefore, it is clear that the EPR line originated from the carbon radicals' centers at the π-network plane rather than other possible radicals [42], [43]. Based on this result, we have enough reason to speculate that the GO may possess the ability to capture the free radicals originated by LMNPs and prolonged their lifespan, therefore effectively initiates the polymerization at room temperature. The formation mechanism of carbon radicals with the existence of LMNPs and GO is shown in the Fig. 4 d. Specifically, the H_2O molecules decompose into $\bullet OH$ radicals in the presence of LMNPs, analogy to the addition reaction occurring with many radical scavengers [44], the $\bullet OH$ radicals immediately add to the double bonds at the GO plane, leading to the formation of π-conjugated carbon radicals. To intuitively demonstrate the existing carbon radicals, the chemiluminescence experiment is conducted in our research by adding luminol agent in the system as shown in Fig. 4 a (II) and (III). When luminol is added to the LMNPs@GO solution under ultrasonication, a blue chemiluminescence is directly observed by the naked eye, which lasted for 20 s (Fig. 4 a (III)). For a comparison, the chemiluminescence for only adding LMNPs (Fig. 4 a (II)) is very weak, indicating the low density of radicals in the system. It is commonly believed that free radicals possessed strong oxidizing properties. Based on this, the oxidation equivalent of the LMNPs@GO is measured by iodometric titration method. As shown in Fig. 4 a (I), the addition of KI and amylum in the LMNPs@GO immediately changes the solution to deep blue which indicates the LMNPs@GO can react with KI to form I2. After the reaction of LMNPs@GO with KI, the resulting iodine is titrated with Na2S2O3 solution. The oxidation equivalent of

LMNPs@GO relative to I2 is evaluated to be 1.12 mmol/g LMNPs@GO and the detailed procedure can be seen in the supporting information.
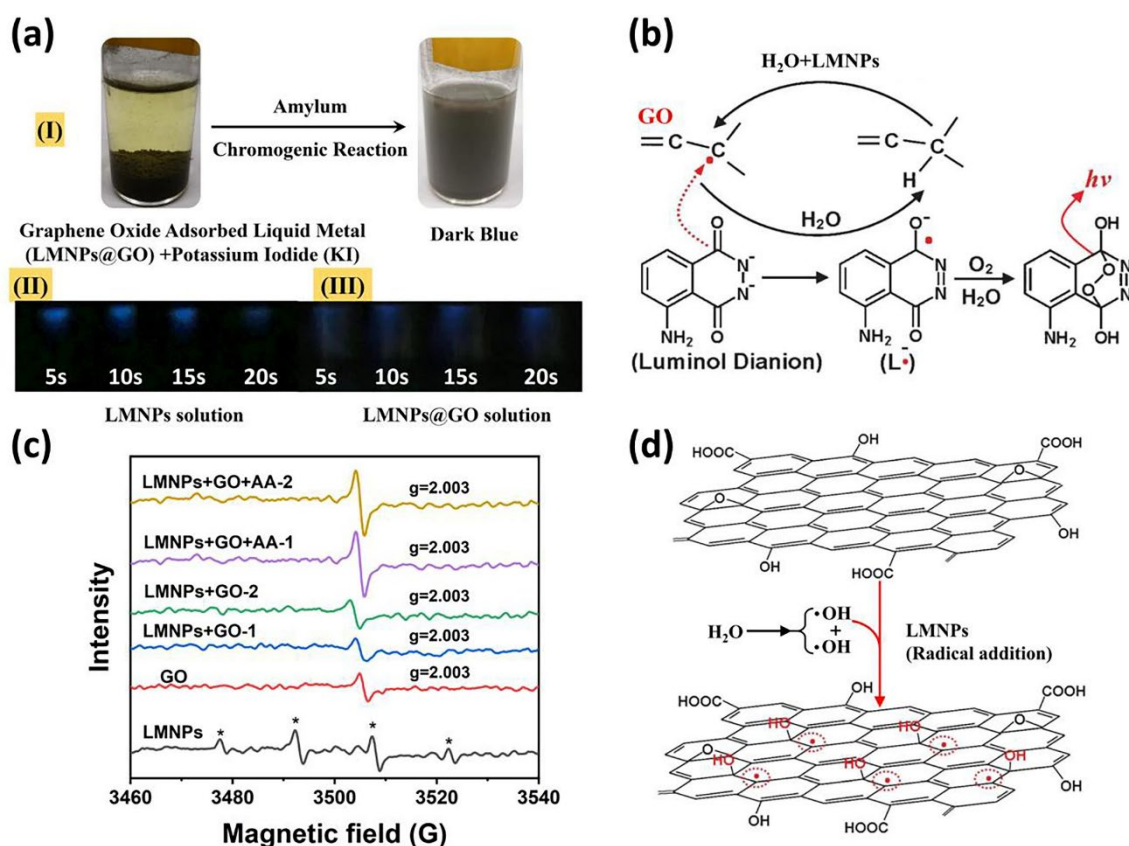

Fig. 4. Characterization of free radicals. (a) Color reaction triggered by the addition of KI and amylum (I). Chemiluminescence of LMNPs solution (II) and LMNPs@GO solution (III) under ultrasonication. (b) The mechanism of the chemiluminescence of luminol triggered by the π-conjugated carbon radicals; (c) EPR spectrum of the spin adduct(s) of DMPO (100 mM) adding in different aqueous solution containing LMNPs, LMNPs + GO and LMNPs + GO + AA, respectively. (d) The proposed mechanism for the formation of π-conjugated carbon radicals by the addition of LMNPs initiated hydroxyl radicals.

As to the speculation (ii) that AA monomers can be adsorbed on the GO nanosheets in aqueous solution, the adsorption energy (Ea) of AA is calculated via Density Functional Theory (DFT) simulations as shown in Fig S8. The Ea of AA on the GO surface is −4.31 eV which is lower than −3.65 eV of graphene sheets (GNPs), indicating that GO possesses stronger capabilities to adsorb AA monomers. It should be noted that the Ea of GNPs here is only a theoretical calculating value. In our experiments, the GNPs is not able be dispersed in water so that it cannot involve in the reaction to initiate the polymerization.

3.4. Mechanical properties

The mechanical properties of the LMNPs@rGO/PAA composite hydrogel are systematically investigated. For comparison, the PAA hydrogel initiated by LMNPs without adding GO is firstly studied. As has been discussed in the section 3.1 in Fig. S4 (b), with the increase of

LMNPs, the tensile strength of the hydrogel declines, which implies the polymerization process is prohibited to some extent because high content of LM is harmful to the dispersion of LMNPs under the same ultrasonic power conditions. The sedimentation and aggregation can be reflected by photos as shown in Fig. S4 (a). Considering that less LMNPs (less than1.5 wt%) can hardly initiate the polymerization of the hydrogel, we choose 1.5 wt% LMNPs as the optimized content, combined with different specific loadings of GO which has been discussed in the section 3.2 to prepare LMNPs@GO/PAA hydrogel. The as prepared LMNPs@rGO/PAA hydrogel shows remarkable mechanical properties, especially high performance in tensile strength and stretchability (Fig. S9 a) which can match state-of-art hydrogel reported in the literature (Table S4). The influence of rGO content on the mechanical properties of LMNPs@rGO/PAA hydrogel (water content 56 wt%) is firstly investigated (pure PAA hydrogel initiated by LMNPs as reference sample). The results show that the tensile strength is inextricably related to the rGO nanosheets content in the hydrogel. As shown in Fig. 5a and b, with the increment of rGO, the tensile strength at the hydrogel break can be adjusted from 195 kPa to 937 kPa, which is much higher than that of pure PAA hydrogel. However, compared to pure PAA hydrogel, the nanosheets bring about a negative effect on elongation at break, indicating the hardening and crosslinking effect triggered by the rGO nanosheets. To demonstrate this, the influence of rGO content on the swelling behavior of the LMNPs@rGO/PAA nanocomposite hydrogels are investigated at room temperature (25°C). Fig. S9 b shows time dependence of the swelling ratios for pure PAA and LMNPs@rGO/PAA hydrogels with different rGO contents. The swelling ratios of pure PAA hydrogel are much higher than those of LMNPs@rGO/PAA, which is attributed to the lower cross-linking density because of the lack of rGO cross-linking point. As for LMNPs@rGO/PAA, the swelling ratio gradually decreases with the increasing of rGO contents which is consistent with the results as many previous literature [45], [46], [47], and the only difference is that the rGO nanosheets not only crosslink the PAA polymer chain via physical crosslinking effect such as hydrogen bonding and chain entanglement but also through coordination bond contributed by LMNPs [48]. To better understand the crosslinking mechanism of rGO nanosheets in the LMNPs@rGO/PAA hydrogel system, cyclic tensile tests are performed. The typical loading–unloading curves of LMNPs@rGO/PAA hydrogels containing 0.5 wt% and 1.5 wt% rGO to different tensile strains are shown in Fig. 5 c and e, and their hysteresis ratio (hr) and residual strain (εr) are summarized in Fig. 5 d and f, respectively. The large hysteresis loops and residual strains can be observed in the curves of LMNPs@rGO/PAA hydrogel containing 0.5 wt% rGO. The εr increases dramatically from 39.3% to 180.4% with increasing tensile strain from 100% to 500%, while the hr keeps almost constant. In comparison, the LMNPs@rGO/PAA hydrogel containing 1.5 wt% rGO exhibits much smaller hysteresis loops and residual strains. When the tensile strain increases from 100% to 500%, the εr increases from 36.2% to 77.1% and hr decreases to a certain extent. The huge differences in the hysteresis ratio and residual strain between the two hydrogels suggest that the LMNPs@rGO/PAA hydrogel with a lower content of rGO possesses a more prominent energy dissipating mechanism than that with a higher rGO content. The reason behind this phenomenon is that the crosslinking effect for hydrogel with higher content of rGO nanosheets provides much more coordination crosslinking points originated from LMNPs@rGO, restricting the segmental motion of PAA chains compared with those with less content of rGO nanosheets. Therefore, the LMNPs@rGO/PAA hydrogel containing 0.5 wt% rGO has a higher hysteresis. In addition, it should be noted that the presence of large residual strain indicates that the damaged physical crosslinking effect cannot be fully

recovered, which implies the incorporation of coordination bond holds inherent advantages in preparing hydrogel with better mechanical performance.
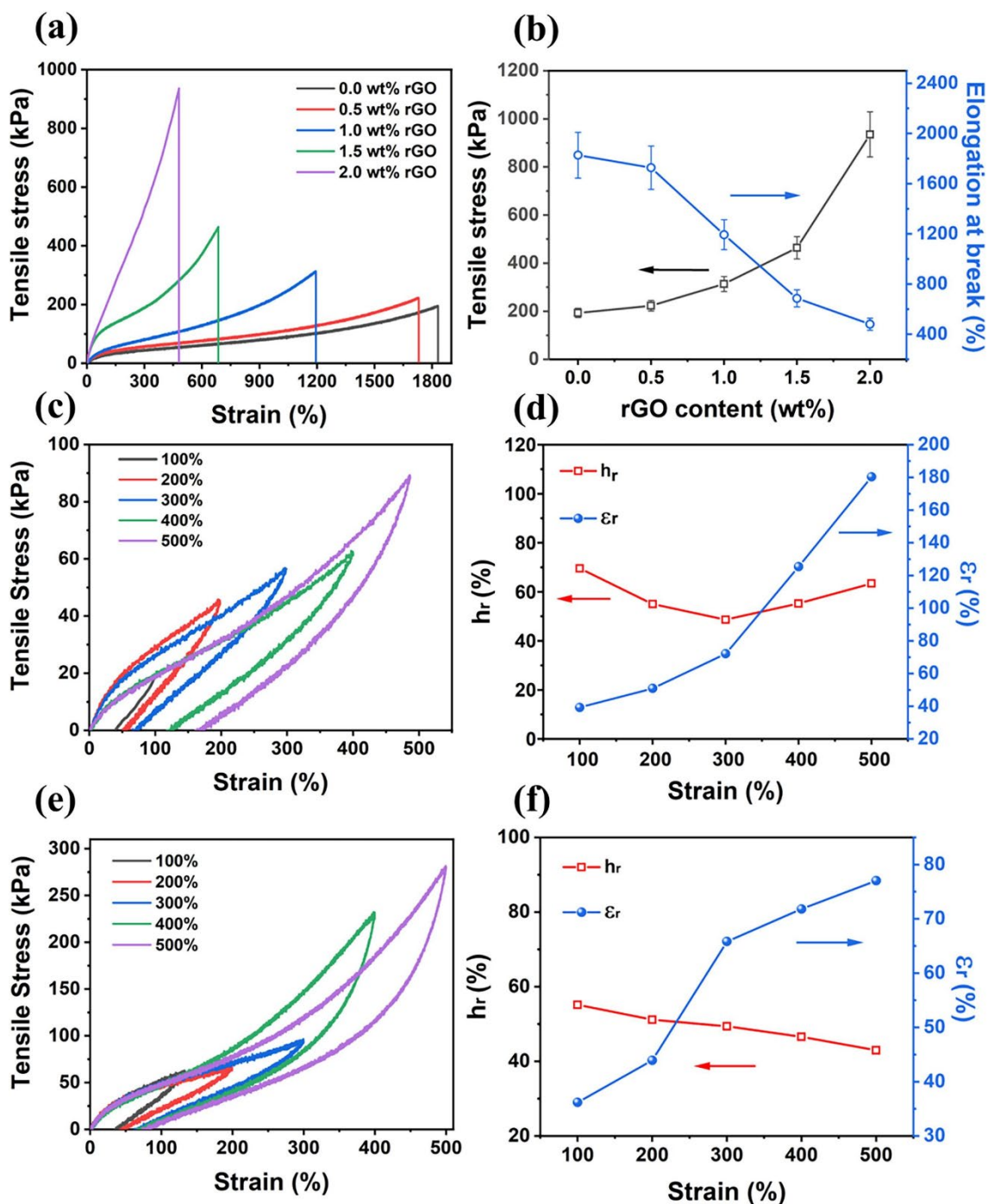

Fig. 5. Mechanical properties of LMNPs@rGO/PAA hydrogel. (a) Typical tensile stress–strain curves of the hydrogel with different rGO loadings. (b) Comparison of tensile strength and break elongation of LMNPs@rGO/PAA hydrogel with varied rGO loadings. (c) Typical tensile loading–unloading curves of the 0.5 wt% LMNPs@rGO/PAA hydrogel and (e) 1.5 wt% LMNPs@rGO/PAA hydrogel to different tensile strains. The corresponding hysteresis ratio (h_r) and residual strain (ε_r) of the 0.5 wt% LMNPs@rGO/PAA hydrogel (d) and 1.5% LMNPs@rGO/PAA hydrogel (f). Cyclic tensile tests were performed with different original specimens.

3.5. Self-healing, conductive and dissolvable properties

Without the assistance of any extra additives such as water or acid, a remarkable self-healing ability can be achieved due to the incorporation of LMNPs combined with other reversible electrostatic interaction and hydrogen bonding in the PAA hydrogel system. The incorporation of LMNPs provides the "containers" which can release Ga3+ during the deformation and rupture of the hydrogel under acidic conditions. Because of the existence of ionic interconnections between the –COO- of PAA and Ga3+, the defect in the section can be healed. As shown in Fig. S10 a, a pristine cylinder of the PAA hydrogel sample is cut into two halves and after exerting some pressure by hand for a while (10 min), the two pieces can be combined again. This result applies equally to the samples of LMNPs@rGO/PAA Fig. S10 b and samples between LMNPs@rGO/PAA and PAA Fig. S10 c, and all healed samples can be stretched to a large strain by hand. The tensile stress–strain curves of three kinds of typical samples before and after self-healing for 24 h are shown in Fig. 6 a and the corresponding healing efficiency is presented in Fig. 6 b. For PAA hydrogel, the fracture stress and strain are healed to 83% (162 kPa) and 76.5% (1396%) of its original state (195 kPa, 1825%), respectively. After addition of 1.5 wt% rGO, the fracture stress and strain of the hydrogel recover to 95.5% (445 kPa) and 65.8% (450%) of the original value (465 kPa, 685%). Further increase of rGO content (2 wt%) seems to reduce the recovery efficiency but the healing value for stress and strain still maintain a high-level standard of 62.2% (578 kPa) and 68.5% (332%). This result demonstrates that the introduction of large amount of GO (2 wt%) may exert negative effect on the self-healing efficiency of PAA hydrogel. The reason behind this phenomenon is as follows: in the as prepared hydrogel system, the Ga3+ released by relatively large size nanodroplets play a dominant role for self-healing properties of the material. The addition of GO can improve the dispersion state of LM in the hydrogel as shown in Fig S5, therefore less large LNMPs are available for rupturing to release Ga3+ to induce the self-healing. Besides, the aggregation and crosslinking effect of rGO nanosheets also hinders the segmental motion of polymer chains and the migration of Ga3+ ions released by LMNPs, therefore, the self-healing efficiency of the PAA hydrogel containing 2 wt% decreases. The stress–strain curves of LMNPs@rGO/PAA hydrogels containing 2 wt% rGO at different waiting times and self-healing efficiency are shown in Fig. 6c and d. These results indicate that in the first few hours (2–10 h) the samples exhibit higher healing efficiency owing to fast diffusion of Ga3+ across the PAA segment, and once the Ga3+ diffusion reaches equilibrium the coordination bonding rate decreases, leading to the decline of self-healing efficiency. It is worth noting that other non-coordinating interactions such as hydrogen bond (Fig. 6 e) also participates in the self-healing process, however, as many other researches demonstrate that without the addition of water, hydrogen bond is not easily formed in a short time [49], [50].
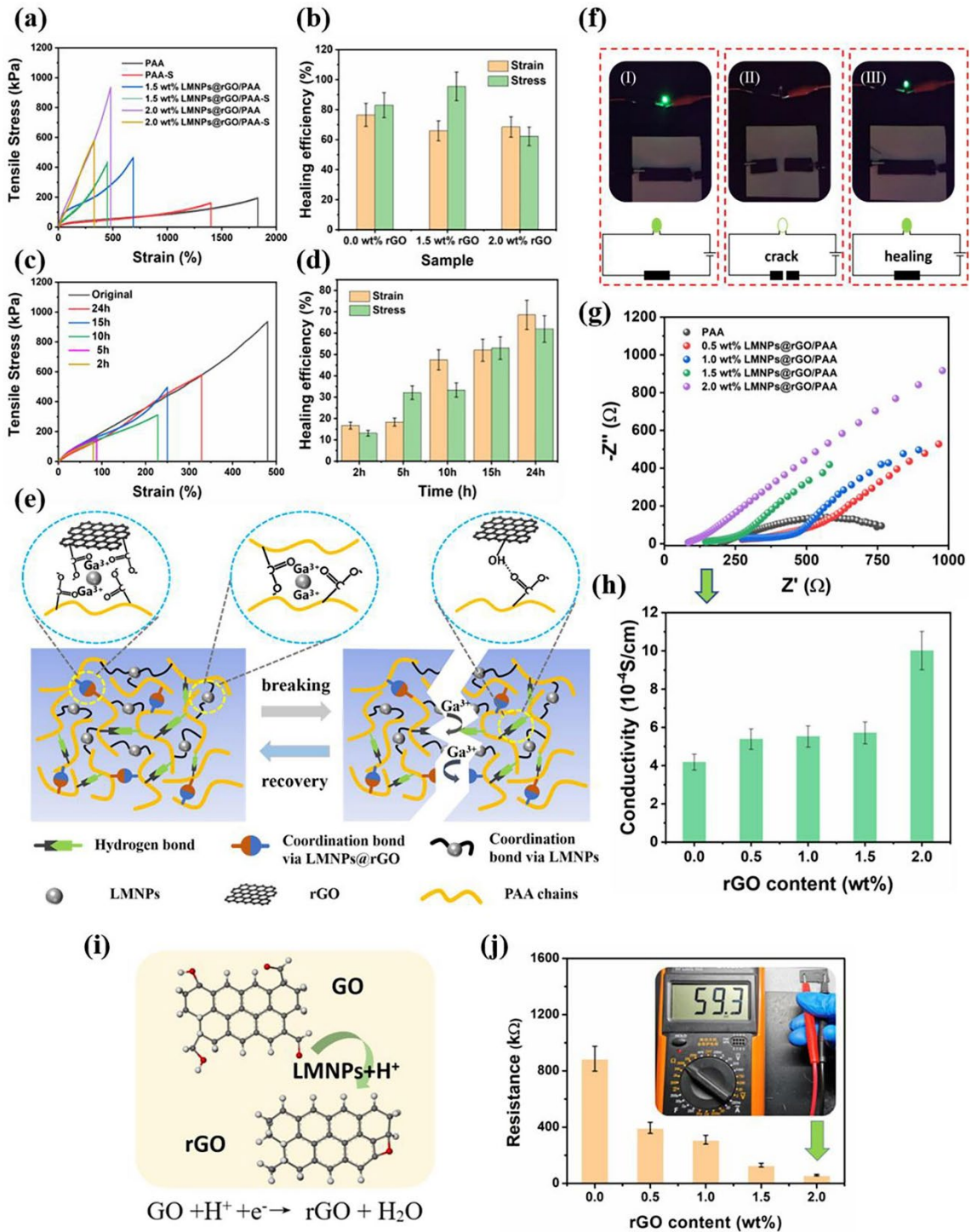
Fig. 6. Self-healing and conductive properties of LMNPs@rGO/PAA hydrogels. (a) Stress–strain curves of representative PAA hydrogels with different rGO content before and after self-healing. (b) Healing efficiency of tensile stress and strain of representative PAA hydrogels with varied rGO contents. (c) Stress–strain curves of PAA hydrogels containing 2 wt% rGO under different self-healing time. (d) Healing efficiency of tensile stress and strain of PAA hydrogels with 2 wt% rGO under different self-healing time. (e) Scheme of self-healing property for LMNPs@rGO/PAA hydrogels. The self-healing property benefits from the coordination and hydrogen bond, and the released Ga+ coming from the ruptured LMNPs. (f) Circuits and cartoons of self-healing LMNPs@rGO/PAA hydrogels connected in series with a green LED indicator. (g) AC impedance spectroscopy of PAA hydrogel with different rGO content. (h) Comparison of ohmic conductivity of PAA hydrogel with different GO content. (i) Schematic diagram of the reduction of GO under acidic condition with

LMNPs. (j) Surface resistance of PAA hydrogel incorporated with different GO content. (the distance between the two electrodes was all fixed at 1 cm).

The non-covalent interaction makes it available for the LMNPs@rGO/PAA hydrogel dissolving in the NaOH solution, which endows the LM with recyclable properties. To demonstrate this, a small piece of sample is placed into the NaOH solution (1 M) at room temperature for different time periods. As shown in Fig. S11 a, the hydrogel can be easily dissolved in the solution within 24 h. This excellent dissolvable property is mainly attributed to the dissociation of coordination bond between Ga3+ and carboxyl groups under alkaline environment. Moreover, the oxide layer on the surface of LMNPs can also be washed as shown in Fig. S12 a, which ensures the recyclability of LM from hydrogel (Fig. S12 b). SEM images of pristine GO and rGO washed by NaOH solution are shown in Fig S11 b and c. it can be observed that compared with pristine GO nanosheets which exhibits ultra-thin 2D structure, the rGO sheet shows thick sheet morphology, indicating the π-π stacking of the nanosheet because of the lack of functional groups. The FTIR spectrum shown in Fig. S11 e proves that the rGO dissolved from the LMNPs@rGO/PAA hydrogel doesn't display prominent characteristic adsorption peak around 1390 cm−1, which indicates that most of the PAA chains is successfully detached from the rGO nanosheet surface. Interestingly, the element Ga can still be observed on the rGO surface as demonstrated by EDS mapping (Fig. S11 d), which provides the evidence that some of the LMNPs can still be strongly adsorbed on the GO (or rGO) before and after polymerization. Based on the results illustrated above, we can conclude that the as prepared LMNPs@rGO/PAA hydrogel exhibits excellent dissolvable properties and some portion of LM can be recycled, which is beneficial for meeting the demand of sustainable development.

The excellent mechanical property and dynamic self-healing feature enable stretchable LMNPs@rGO/PAA composite hydrogel to act as self-healable conductors for flexible circuit. We firstly characterize the surface direct-current (DC) resistance of the hydrogel by fixing the electrodes of the AVO meter with the same distance of 1 cm on the surface of the samples (Fig. 6 j). The results indicate that the resistance of the LMNPs@rGO/PAA hydrogel decreases sharply from 887 kΩ to 59.3 kΩ with the increase of GO addition. This result can also be reflected by the AC impedance test as shown in Fig. 6 g. By extrapolating and fitting the imaginary part of impedance (Z''), the ohmic conductivity can be obtained as shown in Fig. 6h. The results are consistent with the DC resistance test that the volume and surface conductivity of the LMNPs@rGO/PAA hydrogel are all be in direct proportion to the content of the addition of GO. The self-healing capability of LMNPs@rGO/PAA hydrogel for flexible circuit application is presented in Fig. 6 f. As is shown, the LMNPs@rGO/PAA nanocomposite hydrogel is connected in series with a green light LED indicator by a 3 V power supplier. After cutting the hydrogel with the razor blade, the LED bulb goes out in the open circuit. After putting the two bifurcated pieces together and the reformation of the dynamic cross-linking between the contact interfaces of the two bifurcated pieces, the LED bulb is illuminated again. This behavior implies that the LMNPs@rGO/PAA can be applied in the wearable electronic devices. The brightness of LED after healing reduces slightly, which is attributed to the resistance of the sample increasing by 5% as shown in Fig S13.

It is suggested the improvement of the conductivity for the LMNPs@rGO/PAA hydrogel can be attributed to the reduction of GO in the process of preparing LMNPs@rGO/PAA hydrogel. To demonstrate this, the hydrochloric acid (HCL) is used to simulate the reaction environment by adjusting PH = 2. As is illustrated in the section 3.1, the LMNPs are inclined to be wrapped by the GO nanosheets due to the interaction between LMNPs and oxygen-containing functional groups, such as carboxyl and hydroxy on the defect sites of GO [34]. The resulting close contact between GO and LMNPs facilitates the reduction of GO due to the fast electron transport from Ga/Ga3+ to GO sheets (Fig. 6 i). According to the studies previously reported, this reduction process can be expressed as follows [51]:

The conversion from GO to rGO can be characterized by various strategies as shown in Fig S14. As shown in the XRD patterns (Fig S14 a), the diffraction peak of GO at approximately 10° is sharp while the obtained rGO only exhibits broad diffraction peak from 20° to 30°, confirming the incomplete restoration of the graphite crystal structure. Moreover, the diffraction peak of element In can still be observed, indicating the HCl cannot completely react with element In at room temperature, which is consistent with the results as Virolainen et al. reported [52]. Similarly, the corresponding Raman spectra also presents distinct changes. The intensity ratios (ID/IG) of D and G band of GO and rGO show a distinct change from 1.12 to 1.61 (Fig S14 b). Additionally, the C/O ratio of rGO remarkably increases from 2.08 to approximately 5.07 after GO reduction, according to the XPS spectra (Fig S14 c and d), indicating that LMNPs is an effective reducing agents as other types (Table S5). Therefore, LMNPs can effectively reduce GO in acidic aqueous solutions, which provides the basis for the subsequent preparation of conductive LMNPs@rGO/PAA composite hydrogels.

3.6. LMNPs@rGO/PAA hydrogel for strain sensor application

Strain and compress sensitivity are essential elements for sensors to detect human movement. The strain sensitivity of the hydrogel is evaluated by the gauge factor (GF) defined as $GF=(R-R0)/(R0\varepsilon) = \Delta R/(R0\varepsilon)$, where R and R0 are the resistances of the original and stretched hydrogels, respectively, and ε is the applied strain in the stretched direction. The force-sensitivity (S) is evaluated by the slope of the resistance change rate ($\Delta R/R0$) versus applied stress (σ) in the compressed direction, formulized as $S = \delta(\Delta R/R0)/\delta\sigma$ [53]. The relative resistance change ($\Delta R/R0$) of the PAA hydrogel containing 2 wt% rGO under different tensile strains is shown in Fig. 7 g. The $\Delta R/R0$ of the hydrogel changes from 25% to 95% when the strain increases from 21% to 427%, indicating it can detect different variations of strain as a tensile strain sensor. Fig. 7 a displays the fitting curves of the PAA hydrogel containing 2 wt% rGO. The GF are 0.68, 0.18, and 0.04 in 0–100%, 100–200%, and 200–425% strain ranges, respectively, indicating that the hydrogel containing 2 wt% rGO possesses satisfied sensitivity under relatively low strain conditions. To illustrate this, a schematic diagram is shown in Fig S15 (I). A well conductive network consisting of rGO is formed in the original PAA hydrogel containing 2 wt% rGO without stress. With the increase of external tensile force, the overlapped rGO network is gradually broken, resulting in the sharp rise of resistance. However, once the conductive network is destroyed, the variation of the resistance is only dependent on

the deformation of the hydrogel matrix, therefore the GF is not as large as that under low strain range. The same phenomenon can also be observed under compressive mode. The value of S is 3.53 kPa−1 in the low pressure range from 0 kPa to 7 kPa while only a very small S of 0.005 kPa can be achieved from 7 kPa to 12 kPa. The mechanism behind this phenomenon is very different from that of tensile mode. As shown in Fig S15 (II), with the force exerting on the hydrogel, more conductive network can be easily formed because of the overlapping of rGO nanosheets. The content of rGO is limited, therefore more conductive network cannot be formed by applying more compressive force on the hydrogel. Fig. 7 c exhibits that under compressive force exerting by hand, a large resistance variation can be observed which implying its promising application in compressive strain sensors. Furthermore, the responsive time of the LM-hydrogel under compressive force reaches as fast as 440 ms (Fig. 7 d), indicating the rapid responsive feature for the hydrogels. The impact of applied strain rate on the performance of the hydrogel strain sensor is presented in Fig. 7 f. Within the frequency range from 0.5 Hz to 2 Hz under applied strain of 20%, there is only a slight decrease of $\Delta R/R0$, which verifies the stability of the output signals. The test for the hydrogel to sense the repeating strain is also investigated as shown in Fig. 7 e. The relative resistance change of the LMNPs@rGO/PAA strain sensors remains stable after 500 cycles of 15% strain except a slight fluctuation. The insets reveal their excellent reproducibility of the relative resistance change of the hydrogel, corroborating a remarkable electrical stability.
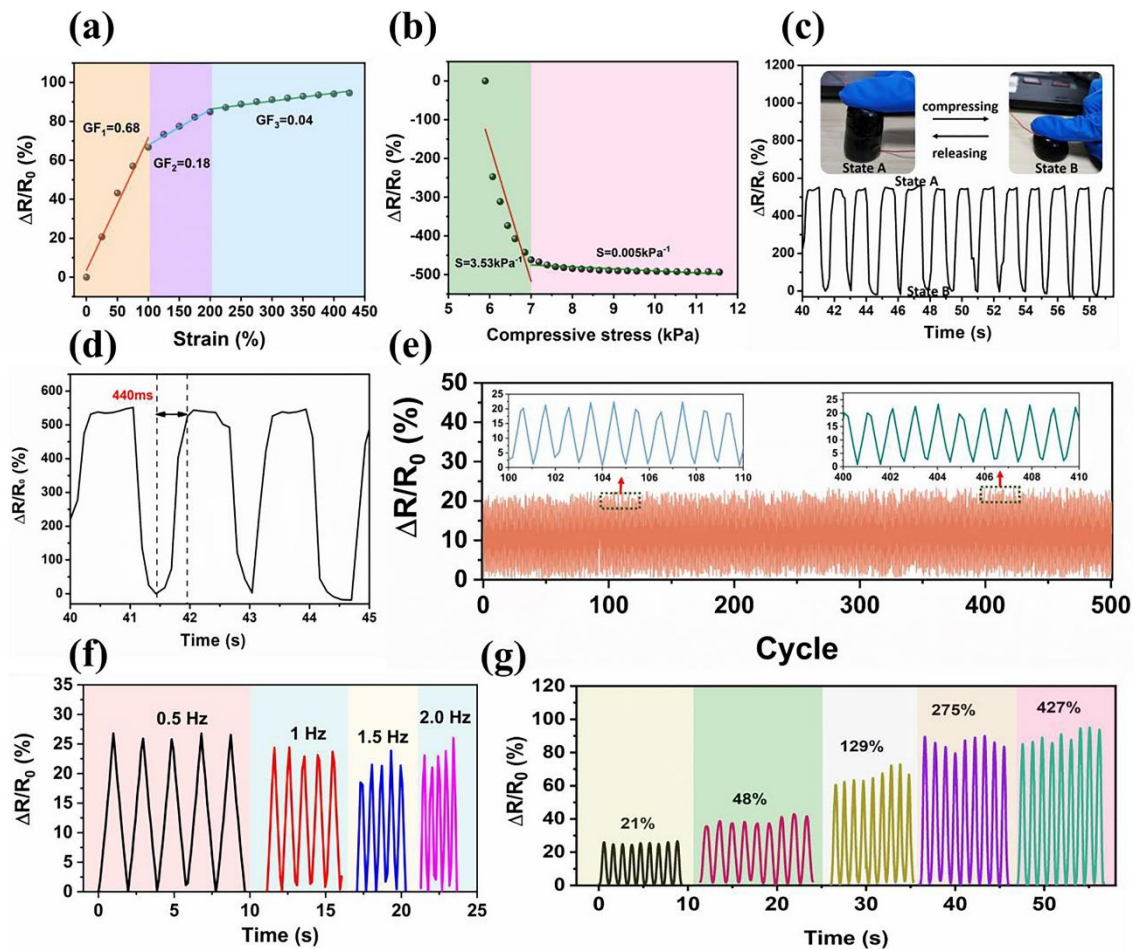

Fig. 7. Sensitive performance of 2 wt% LMNPs@rGO/PAA hydrogel. (a) Relative resistance changes ($\Delta R/R0$) and corresponding gauge factor (GF) variation with successive tensile strain from 0% to 450%; (b) $\Delta R/R0$ and corresponding force-sensitivity (S) variation under different compressive stress. (c) $\Delta R/R0$ under cyclic

compressive stress; (d) response time under compressive mode; (e) cycling test of the hydrogel strain sensor by repeatedly applying a strain of 15% for 500 cycles. (f) $\Delta R/R0$ applied with a strain of 20% under different frequency; (g) $\Delta R/R0$ under cyclic typical different strains.

Based on the good properties of LMNPs@rGO/PAA hydrogel, including excellent mechanical strength, self-healing ability and high sensitivity, it can be directly adhered to human skin to monitor human movement as a strain sensor. Fig. 8 a depicts the $\Delta R/R0$ of fingers with different bending angles. When the bending angle of the finger changes from 0° to 30°, 60°, and 90°, the $\Delta R/R0$ gradually increases from 0% to 11%, 24%, and 39%, respectively. Importantly, the $\Delta R/R0$ can remain stable when the bending angle is constant, indicating that the LMNPs@rGO/PAA hydrogel-based sensor has good stability. The motions of the wrist, knee joints, and elbow can also be accurately monitored as shown in Fig. 8 c-e. In addition to monitoring these large-scale human movements, the LMNPs@rGO/PAA hydrogel can also sense some subtle human movements, such as frowning. Fig. 8 b shows the tiny movement of frowning by attaching the hydrogel to the forehead. Strong signals can still be observed although not as stable as that of large-scale movements. Hence, the LMNPs@rGO/PAA hydrogel-based sensor can be applied to monitor different magnitudes of human movement timely and stably, proving that it has great potential in the field of wearable devices.
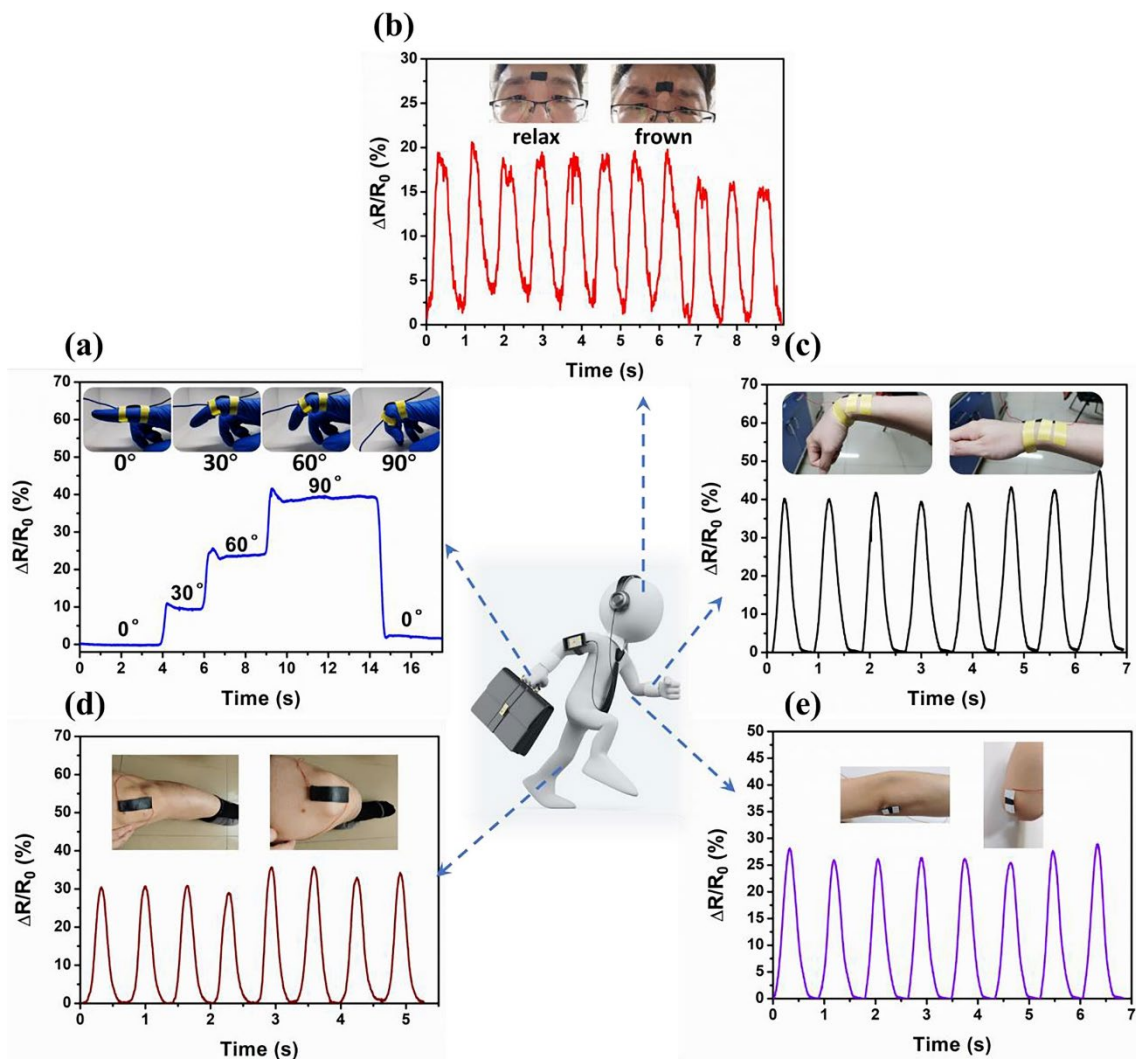
Fig. 8. Real-time monitoring of human physical activities based on wearable sensors assembled from LMNPs@rGO/PAA hydrogel. (a) wrist; (b) frowning; (c) finger; (d) knee. (e) elbow.

4. Conclusion

A multifunctional PAA hydrogel is successfully synthesized via ultra-fast polymerization initiated and crosslinked by LMNPs@GO hybrids. The free-radical polymerization process with LMNPs@GO is extremely faster than that without GO involved: 20 s vs. 4 h of prepolymer formation and then 10 min vs. 3 days of crosslinking for the formation of PAA hydrogels. The resultant hydrogel with 2 wt% rGO exhibits 600% increase in tensile strength and 950% enhancement in conductivity, as well as excellent self-healing capabilities, in comparison with that of the pure PAA. Furthermore, the hydrogel possesses good dissolving properties, which is greatly beneficial for recyclability of the LM. The mechanism behind this fast polymerization phenomenon is systematically investigated combining DFT simulation and free radical capture experiment, and the results show the graphene structure of GO plays the dominant role in accelerating the polymerization process. This creative study not only broadens a novel application of graphene for making advanced multifunctional hydrogels, but also provides a brand-new route to realization of ultra-fast manufacturing technology that is significantly promising for industrial production in wearable devices.

Acknowledgments

References

[1] H.U. Liu, Q. Li, S. Zhang, R. Yin, X. Liu, Y. He, K. Dai, C. Shan, J. Guo, C. Liu, C. Shen, X. Wang, N. Wang, Z. Wang, R. Wei, Z. Guo, Electrically conductive polymer composites for smart flexible strain sensors: a critical review[J], J. Mater. Chem. C 6 (45) (2018) 12121–12141.

[2] Z. Chen, T. Yan, Z. Pan, Review of flexible strain sensors based on cellulose composites for multi-faceted applications[J], Cellulose 28 (2) (2021) 615–645.

[3] S. Li, X. Xiao, J. Hu, M. Dong, Y. Zhang, R. Xu, X. Wang, J. Islam, Recent advances of carbon-based flexible strain sensors in physiological signal monitoring[J], ACS Applied Electronic Materials 2 (8) (2020) 2282–2300.

[4] Z. Ma, H. Li, X. Jing, et al., Recent Advancements in Self-Healing Composite Elastomers for Flexible Strain Sensors: Materials, Healing Systems, and Features[J], Physical, Sensors and Actuators A, 2021, p. 112800.

[5] F. Han, M. Li, H. Ye, G. Zhang, Materials, electrical performance, mechanisms, applications, and manufacturing approaches for flexible strain sensors[J], Nanomaterials 11 (5) (2021) 1220, https://doi.org/10.3390/nano11051220.

[6] Z. Wang, Y. Cong, J. Fu, Stretchable and tough conductive hydrogels for flexible pressure and strain sensors[J], J. Mater. Chem. B 8 (16) (2020) 3437–3459.

[7] D. Zhang, B. Ren, Y. Zhang, L. Xu, Q. Huang, Y.i. He, X. Li, J. Wu, J. Yang, Q. Chen, Y. Chang, J. Zheng, From design to applications of stimuli-responsive hydrogel strain sensors[J], J. Mater. Chem. B 8 (16) (2020) 3171–3191.

[8] X. Sun, F. Yao, J. Li, Nanocomposite hydrogel-based strain and pressure sensors: a review[J], J. Mater. Chem. A 8 (36) (2020) 18605–18623.

[9] L.I. Tang, S. Wu, J. Qu, L. Gong, J. Tang, A review of conductive hydrogel used in flexible strain sensor[J], Materials 13 (18) (2020) 3947, https://doi.org/10.3390/ma13183947.

[10] S. Li, X. Zhou, Y. Dong, J. Li, Flexible Self-Repairing Materials for Wearable Sensing Applications: Elastomers and Hydrogels[J], Macromol. Rapid Commun. 41 (23) (2020) 2000444, https://doi.org/10.1002/marc.v41.2310.1002/marc.202000444.

[11] Y.-J. Liu, W.-T. Cao, M.-G. Ma, P. Wan, Ultrasensitive wearable soft strain sensors of conductive, self-healing, and elastic hydrogels with synergistic "soft and hard" hybrid networks[J], ACS Appl. Mater. Interfaces 9 (30) (2017) 25559–25570.

[12] P. Lv, X. Yang, H.K. Bisoyi, H. Zeng, X. Zhang, Y. Chen, P. Xue, S. Shi, A. Priimagi, L. Wang, W. Feng, Q. Li, Stimulus-driven liquid metal and liquid crystal network actuators for programmable soft robotics[J], Mater. Horiz. 8 (9) (2021) 2475–2484.

[13] L. Tang, L. Wang, X. Yang, Y. Feng, Y.U. Li, W. Feng, Poly (N-isopropylacrylamide)-based smart hydrogels: Design, properties and applications[J], Prog. Mater Sci. 115 (2021) 100702, https://doi.org/10.1016/j.pmatsci.2020.100702.

[14] P. Xue, H.K. Bisoyi, Y. Chen, H. Zeng, J. Yang, X. Yang, P. Lv, X. Zhang, A. Priimagi, L. Wang, X. Xu, Q. Li, Near-infrared light-driven shape-morphing of programmable anisotropic hydrogels enabled by mxene nanosheets[J], Angew. Chem. Int. Ed. 60 (7) (2021) 3390–3396.

[15] J. Yang, X. Zhang, X. Zhang, L. Wang, W. Feng, Q. Li, Beyond the visible: bioinspired infrared adaptive materials[J], Adv. Mater. 33 (14) (2021) 2004754, https://doi.org/10.1002/adma.v33.1410.1002/adma.202004754.

[16] L. Wang, H.K. Bisoyi, Z. Zheng, K.G. Gutierrez-Cuevas, G. Singh, S. Kumar, T. J. Bunning, Q. Li, Stimuli-directed self-organized chiral superstructures for adaptive windows enabled by mesogen-functionalized graphene[J], Mater. Today 20 (5) (2017) 230–237.

[17] C. Shao, M. Wang, L. Meng, H. Chang, B.O. Wang, F. Xu, J. Yang, P. Wan, Musselinspired cellulose nanocomposite tough hydrogels with synergistic self-healing, adhesive, and strain-sensitive properties[J], Chem. Mater. 30 (9) (2018) 3110–3121.

[18] H.-R. Lim, H.S. Kim, R. Qazi, Y.-T. Kwon, J.-W. Jeong, W.-H. Yeo, Advanced soft materials, sensor integrations, and applications of wearable flexible hybrid electronics in

healthcare, energy, and environment[J], Adv. Mater. 32 (15) (2020) 1901924, https://doi.org/10.1002/adma.v32.1510.1002/adma.201901924.

[19] H. Ji, X. Song, H. Cheng, L. Luo, J. Huang, C. He, J. Yin, W. Zhao, L.I. Qiu, C. Zhao, Biocompatible in-situ polymerization of multipurpose polyacrylamide-based hydrogels on skin via silver ion catalyzation[J], ACS Appl. Mater. Interfaces 12 (28) (2020) 31079–31089.

[20] Z. Wang, J. Chen, Y. Cong, H. Zhang, T. Xu, L. Nie, J. Fu, Ultra-stretchable strain sensors and arrays with high sensitivity and linearity based on super tough conductive hydrogels[J], Chem. Mater. 30 (21) (2018) 8062–8069.

[21] K.U. Ingold, D.A. Pratt, Advances in radical-trapping antioxidant chemistry in the 21st century: a kinetics and mechanisms perspective[J], Chem. Rev. 114 (18) (2014) 9022–9046.

[22] D. Zhalmuratova, H.-J. Chung, Reinforced gels and elastomers for biomedical and soft robotics applications[J], ACS Appl. Polymer Mater. 2 (3) (2020) 1073–1091.

[23] T. Kim, D.-M. Kim, B.J. Lee, J. Lee, Soft and deformable sensors based on liquid metals[J], Sensors 19 (19) (2019) 4250, https://doi.org/10.3390/s19194250.

[24] M.H. Malakooti, M.R. Bockstaller, K. Matyjaszewski, C. Majidi, Liquid metal nanocomposites[J], Nanoscale Adv. 2 (7) (2020) 2668–2677.

[25] J. Yan, M.H. Malakooti, Z. Lu, Z. Wang, N. Kazem, C. Pan, M.R. Bockstaller, C. Majidi, K. Matyjaszewski, Solution processable liquid metal nanodroplets by surface-initiated atom transfer radical polymerization[J], Nat. Nanotechnol. 14 (7) (2019) 684–690.

[26] M.G. Saborio, S. Cai, J. Tang, M.B. Ghasemian, M. Mayyas, J. Han, M.J. Christoe, S. Peng, P. Koshy, D. Esrafilzadeh, R. Jalili, C.H. Wang, K. Kalantar-Zadeh, Liquid metal droplet and graphene co-fillers for electrically conductive flexible composites[J], Small 16 (12) (2020) 1903753, https://doi.org/10.1002/smll. v16.1210.1002/smll.201903753.

[27] J. Ma, Y. Lin, Y.-W. Kim, Y. Ko, J. Kim, K.H. Oh, J.-Y. Sun, C.B. Gorman, M. A. Voinov, A.I. Smirnov, J. Genzer, M.D. Dickey, Liquid metal nanoparticles as initiators for radical polymerization of vinyl monomers[J], ACS Macro Lett. 8 (11) (2019) 1522–1527.

[28] H. Peng, Y. Xin, J. Xu, H. Liu, J. Zhang, Ultra-stretchable hydrogels with reactive liquid metals as asymmetric force-sensors[J], Mater. Horiz. 6 (3) (2019) 618–625.

[29] H. Ahmad, M. Fan, D. Hui, Graphene oxide incorporated functional materials: A review[J], Compos. B Eng. 145 (2018) 270–280.

[30] R. Nie, J. Wang, L. Wang, Y.u. Qin, P. Chen, Z. Hou, Platinum supported on reduced graphene oxide as a catalyst for hydrogenation of nitroarenes[J], Carbon 50 (2) (2012) 586–596.

[31] M.M. Shahid, P. Rameshkumar, A. Pandikumar, H.N. Lim, Y.H. Ng, N.M. Huang, An electrochemical sensing platform based on a reduced graphene oxide–cobalt oxide nanocube@platinum nanocomposite for nitric oxide detection[J], J. Mater. Chem. A 3 (27) (2015) 14458–14468.

[32] L. Yang, R. Zhang, B. Liu, J. Wang, S. Wang, M.-Y. Han, Z. Zhang, π-conjugated carbon radicals at graphene oxide to initiate ultrastrong chemiluminescence[J], Angew. Chem. 126 (38) (2014) 10273–10277.

[33] L.Z. Pei, L.J. Yang, Y.P. Dong, J.F. Wang, C.G. Fan, S.B. Wang, J. Chen, W.Y. Yin, Q.-F. Zhang, Large-scale synthesis of submicron gallium oxide hydrate rods and their optical and electrochemical properties[J], Cryst. Res. Technol. 45 (10) (2010) 1087–1093.

[34] C. Ladd, J.-H. So, J. Muth, M.D. Dickey, 3D printing of free-standing liquid metal microstructures[J], Adv. Mater. 25 (36) (2013) 5081–5085.

[35] Y. Wang, S. Wang, H. Chang, W. Rao, Galvanic replacement of liquid metal/reduced graphene oxide frameworks[J], Adv. Mater. Interfaces 7 (19) (2020) 2000626, https://doi.org/10.1002/admi.v7.1910.1002/admi.202000626.

[36] O. Oloye, C. Tang, A. Du, G. Will, A.P. O'Mullane, Galvanic replacement of liquid metal galinstan with Pt for the synthesis of electrocatalytically active nanomaterials[J], Nanoscale 11 (19) (2019) 9705–9715.

[37] J. Xu, Z. Wang, J. You, X. Li, M. Li, X. Wu, C. Li, Polymerization of moldable selfhealing

hydrogel with liquid metal nanodroplets for flexible strain-sensing devices[J], Chem. Eng. J. 392 (2020) 123788, https://doi.org/10.1016/j.cej.2019.123788.

[38] Y. Su, G. Sui, J. Lan, X. Yang, A highly stretchable dielectric elastomer based on

core–shell structured soft polymer-coated liquid-metal nanofillers[J], Chem. Commun. 56 (78) (2020) 11625–11628.

[39] X. Li, M. Li, Q. Shou, L.I. Zhou, A. Ge, D. Pei, C. Li, Liquid metal initiator of ring opening polymerization: self-capsulation into thermal/photomoldable powder for multifunctional composites[J], Adv. Mater. 32 (43) (2020) 2003553, https://doi.org/10.1002/adma.v32.4310.1002/adma.202003553.

[40] E. Walger, N. Marlin, G. Mortha, et al., Hydroxyl radical generation by the H2O2/Cu(II)/phenanthroline system under both neutral and alkaline conditions: an EPR/Spin-Trapping Investigation[J], Applied Sciences 11 (2) (2021) 687.

[41] Q. Zhou, Z. Luo, G. Li, S. Li, EPR detection of key radicals during coking process of lignin monomer pyrolysis[J], J. Anal. Appl. Pyrol. 152 (2020) 104948, https://doi.org/10.1016/j.jaap.2020.104948.

[42] M. Kempiński, S. Ło's, P. Florczak, W. Kempiński, S. Jurga, EPR and Impedance

measurements of graphene oxide and reduced graphene oxide[J], Acta Phys. Pol. A 132 (1) (2017) 81–85.

[43] K. Tadyszak, A. Musiał, A. Ostrowski, J.K. Wychowaniec, Unraveling origins of EPR

spectrum in graphene oxide quantum dots[J], Nanomaterials 10 (4) (2020) 798, https://doi.org/10.3390/nano10040798.

[44] N. Smirnoff, Q.J. Cumbes, Hydroxyl radical scavenging activity of compatible solutes[J], Phytochemistry 28 (4) (1989) 1057–1060.

[45] M. Zhong, Y.-T. Liu, X.-M. Xie, Self-healable, super tough graphene oxide–poly (acrylic acid) nanocomposite hydrogels facilitated by dual cross-linking effects through dynamic ionic interactions[J], J. Mater. Chem. B 3 (19) (2015) 4001–4008.

[46] L. Zhao, J. Huang, T. Wang, W. Sun, Z. Tong, Multiple shape memory, selfhealable, and super tough PAA-GO-Fe3+ Hydrogel[J], Macromol. Mater. Eng. 302 (2) (2017) 1600359, https://doi.org/10.1002/mame.v302.210.1002/ mame.201600359.

[47] A. Ma, C. Jiang, M. Li, L. Cao, Z. Deng, L. Bai, W. Wang, H. Chen, H. Yang, D. Wei, Surface-initiated photoinduced electron transfer ATRP and mussel-inspired chemistry: Surface engineering of graphene oxide for self-healing hydrogels[J], React. Funct. Polym. 150 (2020) 104547, https://doi.org/10.1016/j.reactfunctpolym.2020.104547.

[48] M. Wang, Z. Lai, X. Jin, T. Sun, H. Liu, H. Qi, Multifunctional liquid-free ionic conductive elastomer fabricated by liquid metal induced polymerization[J], Adv. Funct. Mater. 31 (32) (2021) 2101957, https://doi.org/10.1002/adfm.v31.3210.1002/adfm.202101957.

[49] D.L. Taylor, M. in het Panhuis, Self-healing hydrogels[J], Adv. Mater. 28 (41)

(2016) 9060–9093.

[50] A. Phadke, C. Zhang, B. Arman, C.-C. Hsu, R.A. Mashelkar, A.K. Lele, M.J. Tauber,

G. Arya, S. Varghese, Rapid self-healing hydrogels[J], Proc. Natl. Acad. Sci. 109 (12) (2012) 4383–4388.

[51] Z. Zhang, L. Tang, C. Chen, H. Yu, H. Bai, L. Wang, M. Qin, Y. Feng, W. Feng, Liquid

metal-created macroporous composite hydrogels with self-healing ability and multiple sensations as artificial flexible sensors[J], J. Mater. Chem. A 9 (2) (2021) 875–883.

[52] S. Virolainen, D. Ibana, E. Paatero, Recovery of indium from indium tin oxide by

solvent extraction[J], Hydrometallurgy 107 (1-2) (2011) 56–61.

[53] Q. Jiao, L. Cao, Z. Zhao, H. Zhang, J. Li, Y. Wei, Zwitterionic hydrogel with high transparency, ultrastretchability, and remarkable freezing resistance for wearable strain sensors[J], Biomacromolecules 22 (3) (2021) 1220–1230.